



Degradation mechanisms of perovskite solar cells under vacuum and one atmosphere of nitrogen

Renjun Guo^{1,11}, Dan Han^{2,11}, Wei Chen^{1,3,11}, Linjie Dai⁴, Kangyu Ji⁴, Qiu Xiong⁵, Saisai Li⁶, Lennart K. Reb¹, Manuel A. Scheel¹, Shambhavi Pratap¹, Nian Li¹, Shanshan Yin¹, Tianxiao Xiao¹, Suzhe Liang¹, Anna Lena Oechsle¹, Christian L. Weindl¹, Matthias Schwartzkopf⁷, Hubert Ebert², Peng Gao⁵, Kai Wang³, Mingjian Yuan⁶, Neil C. Greenham⁴, Samuel D. Stranks^{4,8}, Stephan V. Roth^{7,9}, Richard H. Friend⁴ and Peter Müller-Buschbaum^{1,10}✉

Extensive studies have focused on improving the operational stability of perovskite solar cells, but few have surveyed the fundamental degradation mechanisms. One aspect overlooked in earlier works is the effect of the atmosphere on device performance during operation. Here we investigate the degradation mechanisms of perovskite solar cells operated under vacuum and under a nitrogen atmosphere using synchrotron radiation-based operando grazing-incidence X-ray scattering methods. Unlike the observations described in previous reports, we find that light-induced phase segregation, lattice shrinkage and morphology deformation occur under vacuum. Under nitrogen, only lattice shrinkage appears during the operation of solar cells, resulting in better device stability. The different behaviour under nitrogen is attributed to a larger energy barrier for lattice distortion and phase segregation. Finally, we find that the migration of excessive PbI_2 to the interface between the perovskite and the hole transport layer degrades the performance of devices under vacuum or under nitrogen.

Solution-processed hybrid halide perovskite materials have attracted strong interest for next-generation thin-film photovoltaic applications due to their high power conversion efficiency (PCE) and low fabrication costs compared with silicon photovoltaics¹. With solvent engineering, compositional tuning and surface passivation^{2–4}, the highest PCE of perovskite solar cells (PSCs) has reached 25.5% (ref. ⁵). Moreover, the possibility of fabricating PSCs on flexible substrates opens up promising manufacturing routes, and novel application fields can be explored, such as lightweight photovoltaic devices for space applications. Previous studies showed that PSCs were successfully operated in space with low vacuum conditions, such as on a high-altitude balloon and a suborbital rocket^{6–8}. Although these pioneering studies confirmed the possibility of operating PSCs in space, the operational stability of PSCs under such conditions is unknown. In terrestrial studies, vacuum conditions play a major role in the performance loss of PSCs during operation. Thus, although there is such a rapid increase in the PCE, very important challenges remain. More research is required to increase the stability of materials and the longevity of devices, as long-term operational stability remains the main challenge for real-world applications of hybrid halide perovskite materials. Therefore, investigating the performance degradation mechanism of PSCs under different atmospheric conditions is one approach that is important to further improve the long-term operational stability of PSCs⁹.

Exposure to above-band-gap illumination can cause a loss of phase and structure stability for perovskite materials. For instance, phase segregation introduced by lattice distortion, halide migration and crystalline reorganization can cause an open-circuit voltage penalty arising from halide segregation¹⁰. In addition, several studies have indicated that a lattice distortion under illumination originates from light excitation or thermal expansion^{11–13}. Although these studies discuss light-induced phase and lattice behaviours, all experiments were executed under different atmospheres and were based on different perovskite systems and architectures. For these reasons, the results of these studies are inadequate for a comprehensive understanding of the mechanisms of light-induced lattice effects by themselves, and there is a need for complementary data. There is no doubt that different macroscopic operation conditions (especially different atmospheres) can profoundly influence the microscopic behaviour of PSCs¹⁴. To this end, Khenkin and co-workers proposed experimental procedures based on the International Summit on Organic Photovoltaic Stability (ISOS) protocols¹⁵. Although the ISOS protocol suggests using a vacuum or inert nitrogen atmosphere as the standard, the effects of these two conditions on the morphology and optoelectronic properties of PSCs have not yet been investigated systematically. To direct scientific progress towards commercial applications, the degradation mechanism of PSCs, specifically including their microscopic and macroscopic behaviour, needs to be fully understood under vacuum and under a nitrogen atmosphere.

¹Lehrstuhl für Funktionelle Materialien, Physik-Department, Technische Universität München, Garching, Germany. ²Department Chemie, Ludwig-Maximilians-Universität München, Munich, Germany. ³Department of Electrical and Electronic Engineering, Southern University of Science and Technology, Shenzhen, China. ⁴Cavendish Laboratory, University of Cambridge, Cambridge, UK. ⁵Fujian Institute of Research on the Structure of Matter, Chinese Academy of Sciences, Fuzhou, China. ⁶Department of Chemistry, Nankai University, Tianjin, China. ⁷Deutsches Elektronen-Synchrotron (DESY), Hamburg, Germany. ⁸Chemical Engineering and Biotechnology, University of Cambridge, Cambridge, UK. ⁹Department of Fiber and Polymer Technology, KTH Royal Institute of Technology, Stockholm, Sweden. ¹⁰Heinz Maier-Leibnitz-Zentrum, Technische Universität München, Garching, Germany. ¹¹These authors contributed equally: Renjun Guo, Dan Han, Wei Chen. ✉e-mail: muellerb@ph.tum.de

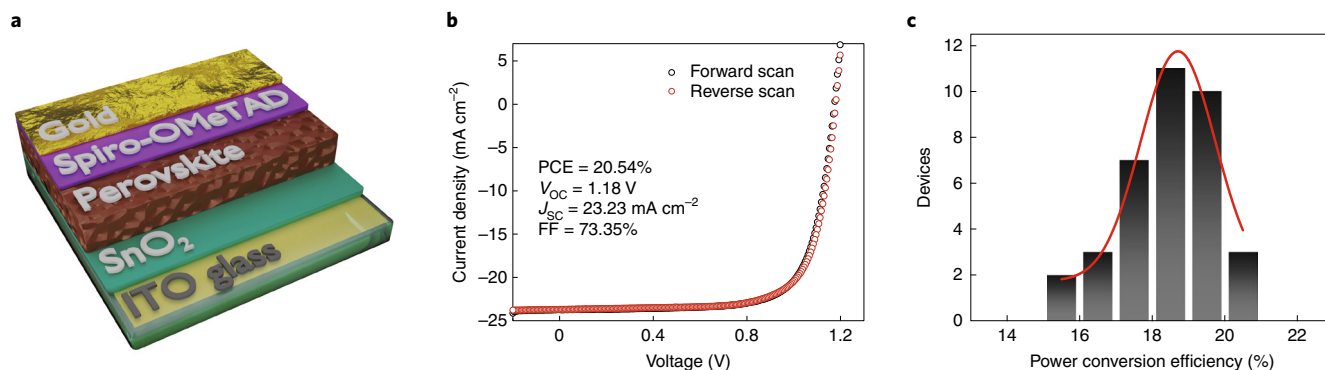


Fig. 1 | Structure and performance of the devices analysed. **a**, Sketch of the device architecture of fabricated planar MAFA perovskite solar cells. **b**, J - V scan of the champion device for MAFA perovskite solar cells and related device parameters. **c**, Histogram of PCE obtained from 36 fabricated MAFA PSCs with the red line displaying a Gaussian fit.

Here, we report that mixed-cation mixed-halide lead perovskite ($(\text{MAPbBr}_3)_{0.17}(\text{FAPbI}_3)_{0.83}$ (MAFA) PSCs (MA, methylammonium; FA, formamidinium) experience a remarkable lattice shrinkage, a phase segregation into a FAPbI_3 phase as the minority phase and a large amount of $(\text{MAPbBr}_3)_{0.17+x}(\text{FAPbI}_3)_{0.83-x}$ as the majority phase for the perovskite layer, under standard one-Sun illumination (AM 1.5G) in vacuum. The intrinsically different crystallite orientations of the two perovskite phases offer a pathway for phase segregation. Meanwhile, the phase segregation of the perovskite materials introduces a coherent phase boundary to decrease the film strain. In contrast, continuous operation in nitrogen under the same illumination intensity has only a minor effect on the lattice dynamics of the perovskite materials. Thus, atmosphere affects the deterioration of the morphology of the perovskite layer. Calculations using density functional theory (DFT) reveal that the thermodynamic driving force for lattice distortion and phase segregation of the perovskite material is highly atmosphere-dependent. Experimental results and device simulations together prove the relationship between physical changes and device performance. We highlight the obvious effects of atmosphere on the degradation pathways of the devices, even with the applied ISOS protocol.

Device performance and material characterization

We fabricated planar MAFA PSCs via the anti-solvent method, as previously reported¹⁶. Figure 1a presents the device architecture of the studied PSCs. The PCE of the champion device equals the certified record for MAFA perovskite solar cells (Fig. 1b)¹⁷. Figure 1c shows the related histogram of the PCE data for 36 devices. The narrow steady-state photoluminescence spectrum and the sharp edge in the absorbance spectrum for MAFA perovskite films suggest uniformity and phase purity (Supplementary Fig. 1a)¹⁸. Top-view scanning electron microscopy (SEM) and cross-section SEM images show smooth perovskite films, indicating the formation of condensed grains without pinholes (Supplementary Fig. 1b,c). X-ray diffraction data (Supplementary Fig. 2a,b) show Bragg reflexes from δ - FAPbI_3 and PbI_2 phases. The existence of these phases in perovskite films was reported to boost the PCE of perovskite solar cells^{19,20}; however, an excessive amount of PbI_2 leads to poor device performance²¹. These material properties and device efficiencies are of critical importance for this state-of-the-art research of degradation.

Structural changes during operation of the devices

Through operando grazing-incidence wide-angle X-ray scattering (GIWAXS) studies on the MAFA PSCs via the ISOS-L-II protocol (with continuous voltage-bias scan and illumination in inert

atmospheres), we find different extents of lattice shrinkage under different atmospheres. Pictures of the operando set-up are shown in Supplementary Fig. 3. The detailed experimental conditions and data treatment are listed in the Methods section and Supplementary Note 1. The scattering depth for the MAFA perovskite is 660 nm at the incident angle used of 0.4° , which ensures that we measure the statistical bulk information of the PSCs (Supplementary Fig. 6 and Supplementary Note 2).

Under vacuum, the time evolution of two-dimensional (2D) GIWAXS data demonstrates a remarkable lattice shrinkage and phase segregation into the minority phase FAPbI_3 and the majority phase $(\text{MAPbBr}_3)_{0.17+x}(\text{FAPbI}_3)_{0.83-x}$ during the operation of the PSCs (Fig. 2a,c). The (100) Bragg peak position of the MAFA perovskite experiences a dramatic shift after 45 min of illumination (increasing from 0.998 \AA^{-1} to 1.018 \AA^{-1}), proving a dramatic decrease of the interplane spacing of the crystal. This initial shift of the (100) Bragg peak position is followed by a slight back shift (decreasing from 1.018 \AA^{-1} to 1.010 \AA^{-1}), coinciding with the phase segregation as seen in the (210) Bragg peak. In contrast, the time evolution of the line profiles, azimuthally integrated from the 2D GIWAXS scattering data, indicates that the MAFA perovskite undergoes only a slight lattice shrinkage in nitrogen (Fig. 2b). Since different Bragg peaks reflect different lattice spacings in the materials, we assign the Bragg peak (hkl) of the cubic structure with the following equation:

$$d_{hkl} = a\sqrt{h^2 + k^2 + l^2} \quad (1)$$

where a , d_{hkl} and (h, k, l) refer to the lattice parameters, interplanar spacing and Miller indices, respectively. According to the cubic model, the degree of lattice shrinkage extracted from the (110) and (111) Bragg peaks is different from that for the measured data of the (100) Bragg peak for the whole illumination period (Fig. 2d and Supplementary Fig. 7a,b). Therefore, the lattice shrinkage of the MAFA perovskite is non-uniform under operation in both atmospheres because the lattice constants are different in different lattice planes. In addition, Supplementary Fig. 7c shows that the emergence of Bragg peaks around 1.6 \AA^{-1} indicates the formation of the tetragonal perovskite phase caused by a non-uniform lattice shrinkage, which was also found in a previous study due to a composition change²².

We further use the Williamson–Hall analysis for azimuthally integrated line profiles to track the film strain evolution under both atmospheres (Supplementary Notes 3 and 4, and Supplementary Fig. 8). During the operation of PSCs under vacuum, the strain of the MAFA perovskite layer increases first, then decreases slightly after the phase segregation into a minority phase FAPbI_3 , and a

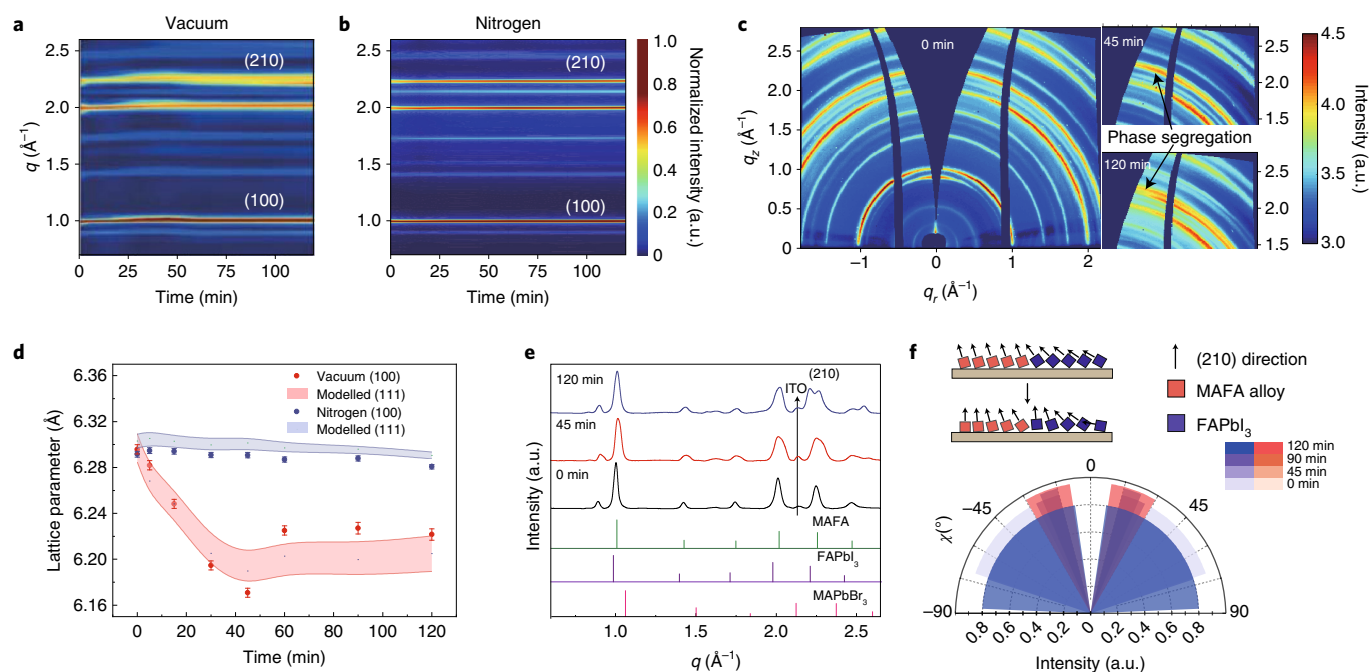


Fig. 2 | Structure evolution of MAFA PSCs operating in different atmospheres. **a,b**, Time evolution of operando synchrotron radiation-based GIWAXS data plotted as azimuthally integrated line profiles of 2D GIWAXS data for the operation of MAFA PSCs under vacuum (**a**) and in nitrogen (**b**) based on the ISOS-L-1I protocol. **c**, Temporal evolution of 2D GIWAXS data transferred to q -space and collected under vacuum during the operation of the solar cell for 0, 45 and 120 min. **d**, Lattice evolution for different atmospheres (vacuum in red, nitrogen in blue) as a function of illumination time. Filled circles denote the measurements with error bars derived from three-times fit through the Gaussian distribution of the (100) Bragg peak. The shaded areas display the modelled (111) peaks, reflecting a non-uniform shrinkage for all lattice directions. **e**, Evolution of radial GIWAXS profiles integrated over all azimuthal angles (pseudo-X-ray diffraction profiles) during operation for MAFA PSCs in vacuum, and simulated MAFA, FAPbI₃ and MAPbBr₃ perovskite X-ray diffraction scattering patterns. **f**, Crystallite orientation evolution during operation for MAFA perovskite under vacuum (stronger colour patterns indicate the orientation of crystals after longer operation times) reconstructed from the tube cuts of the 2D GIWAXS data at the (210) Bragg peak. The schematic diagram shows the evolution of the crystallite orientation.

majority phase (MAPbBr₃)_{0.17+x}(FAPbI₃)_{0.83-x} appears. In contrast, the film strain releases slightly under operation in a nitrogen atmosphere, and is lower than the film strain found in vacuum. In addition, the (210) Bragg peak of MAFA splits up with the increase of the operation time under vacuum, indicating a phase segregation and the formation of the new components MAFA and FAPbI₃ as a result of 45-min operation under vacuum (Fig. 2e)²³. The release of the film strain happens with phase segregation at the (210) plane, indicating that this plane is the habit plane due to its low film strain²⁴. We calculate the misfit of the separated (210) Bragg peaks at 120 min by using equation (2):

$$\delta = \frac{2(d_{\text{FAPbI}_3} - d_{\text{MAFA}})}{d_{\text{FAPbI}_3} + d_{\text{MAFA}}} \quad (2)$$

We obtain $\delta = 0.022$ (< 0.05), which is the certification of the formation of a coherent phase boundary²⁵. Coherent phase boundaries have a lower energy and can enhance the strength and phase stability of the MAFA perovskite layer²⁶. Although condensed grains are observed by SEM imaging, a local crystal misorientation may exist and produce a local structural strain. Thus, a potential phase segregation would be driven by such local crystal misorientations²⁷. Such a scenario is also confirmed by Supplementary Fig. 9a, which shows that FAPbI₃ crystallite orientations already exist before the phase segregation. This finding indicates that the crystallite orientations of MAFA perovskite films occur already during the fabrication process, which will drive the phase segregation under operation. The broadening of the crystallite orientations as shown in Fig. 2f and Supplementary Fig. 9b–e with increasing operation time indicates

that the orientations of both the MAFA and FAPbI₃ become more disordered after continuous operation.

The results from measurements on top of the gold, top contact also confirm that the structural evolution is not affected by whether the monitoring positions are on the electrode or just beside the electrode (Supplementary Fig. 4a–c,f). When PSCs operate under the ISOS-L-2I protocol with an increased temperature (55 °C) in nitrogen, the perovskite lattice shows a slightly stronger lattice shrinkage tendency (Supplementary Fig. 4d,g). Supplementary Fig. 4e,h confirms that the PbI₂ and δ -FAPbI₃ phases are less likely to affect the lattice distortion because PSCs with the pure-phase component Cs₁₀FA₉₀PbI₃ also experience a lattice shrinkage under operational conditions (ISOS-L-1I). According to the above observations, we believe that the mixed-cation lead mixed-halide perovskites experience lattice shrinkages and phase segregation during the operation of the PSCs.

Morphology changes under operation of devices

We use grazing-incidence small-angle X-ray scattering (GISAXS) to investigate the morphology evolution of PSCs under operation in different atmospheres (Fig. 3a,d). To quantify our results from the 2D GISAXS data, we survey the temporal evolution of the intensities in the horizontal line cuts and model these data with form and structure factors (Supplementary Fig. 10). The superposition of Gaussian distributed form factors used for modelling the GISAXS data relates to the crystal size distribution because the intensity scales linearly

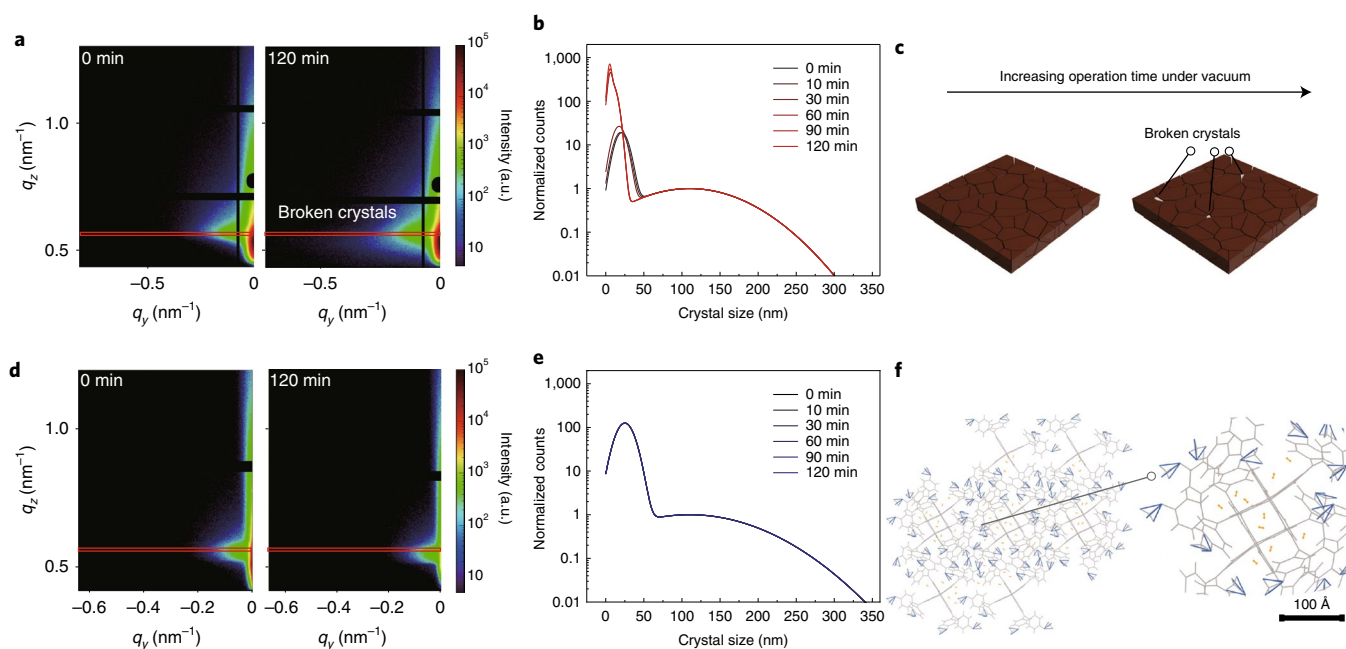


Fig. 3 | Morphology evolution of MAFA PSCs operating in different atmospheres. **a**, Time evolution of 2D GISAXS data under operation in vacuum (red line indicates the horizontal line cut at the perovskite Yoneda peak position). **b**, Evolution of crystal size distributions under operation in vacuum for different form factors extracted from the model and intensity normalized to form factor 1 (~110 nm). **c**, Scheme to illustrate the improved strength of the perovskite film to suppress further deformation through the increase of grain boundaries due to broken crystals. **d**, Time evolution of 2D GISAXS data under operation in a nitrogen atmosphere (red line indicates the horizontal cut at the perovskite Yoneda peak position). **e**, Evolution of crystal size distributions under operation in a nitrogen atmosphere for different form factors extracted from the model and normalized to form factor 1 (~110 nm). **f**, Schematic diagram of nitrogen molecules (yellow symbols) diffusing through the spiro-OMeTAD layer expressed by a blue (side chains) and grey (intermolecular π - π stacking) mixed space frame during the operation of solar cells under nitrogen. The zoomed-in inset indicates the loose structures of spiro-OMeTAD allowing the diffusion of nitrogen molecules.

with the number of crystals of a specific size (Supplementary Notes 5 and 6). Figure 3b,c shows that the number of small crystals increases during operation under vacuum. Our results show that crystals with diameters lower than 40 nm break into smaller crystals. These small crystals act as pinholes in the PSCs²⁸. The increasing number of crystals also introduces an increasing number of grain boundaries. This phenomenon is known as grain-boundary strengthening, which can in turn increase the strength of the MAFA perovskite film under operation in vacuum²⁹. It can stop further degradation of the MAFA perovskite film. In contrast, we do not observe a similar phenomenon in nitrogen (Fig. 3e).

Eperon et al. showed the existence of porosity in the perovskite film using a gas pycnometer, and this porosity could offer a physical pathway for the origin of the nitrogen adsorption process³⁰. To confirm this, we measured the adsorption behaviour of the MAFA perovskite material in nitrogen via the Brunauer–Emmett–Teller method (Supplementary Fig. 11). Indeed, the MAFA perovskite can adsorb more nitrogen as the pressure of nitrogen increases. The perovskite sample exhibits a type III isotherm, which indicates the formation of a nitrogen molecule multilayer around the perovskite layer during the operation of PSCs under nitrogen³¹. For the PSCs used in this study, most of their module area is not covered by electrodes, which means that the majority of the spiro-OMeTAD (2,2',7,7'-tetrakis-(*N,N*-di-4-methoxyphenylamine)-9,9'-spirobifluorene) layer can directly contact the atmosphere. The loose space structure of spiro-OMeTAD offers pathways that allow for the diffusion of nitrogen molecules into the active layer underneath (Fig. 3f). Hence, we suggest that a nitrogen atmosphere under standard pressure helps to stabilize the morphology of the perovskite film during operation. Meanwhile, we highlight

the importance of large crystals for enhancing the stability of perovskite materials.

Mechanisms of atmosphere-dependent operational stability

To investigate the intrinsic driving force for phase segregation and lattice shrinkage, we combine the aforementioned structure and morphology evolution with thermodynamic kinetics to provide an interpretation. For the calculations, we focus on the $(\text{MAPbBr}_3)_{0.2}(\text{FAPbI}_3)_{0.8}$ component. We first use the Gibbs free energy to evaluate the effect of pressure on the free energies of perovskite components, in contrast to a previous report, which applied a GPa-level pressure to suppress the phase segregation of mixed-halide perovskites under illumination³². Atmospheric pressure can only decrease the Gibbs free energy by 1.29×10^{-7} eV due to the use of a relatively low pressure (1.01×10^5 Pa) in our study. Hence, in our study, the increased pressure from the nitrogen atmosphere largely does not affect the free energy and cannot be the reason for the suppression of phase segregation. Thus, we use Helmholtz free energy to calculate the free energy of the mixing perovskite phases. Previous studies have efficiently shown that lattice shrinkage can increase the activation energy barrier to suppress phase segregation due to the decrease in ion migrations³³. However, perovskite films under illumination in vacuum can increase the doping concentration for all hybrid perovskite materials, due to decomposition induced by volatile species or gas desorption-induced defects in the crystal structures³⁴. Simultaneously, the relative permittivity of perovskite materials can change when illumination or pressure are applied^{35,36}. Thus, we recalculated the activation energy of the phase segregation under operation conditions in different atmospheres by

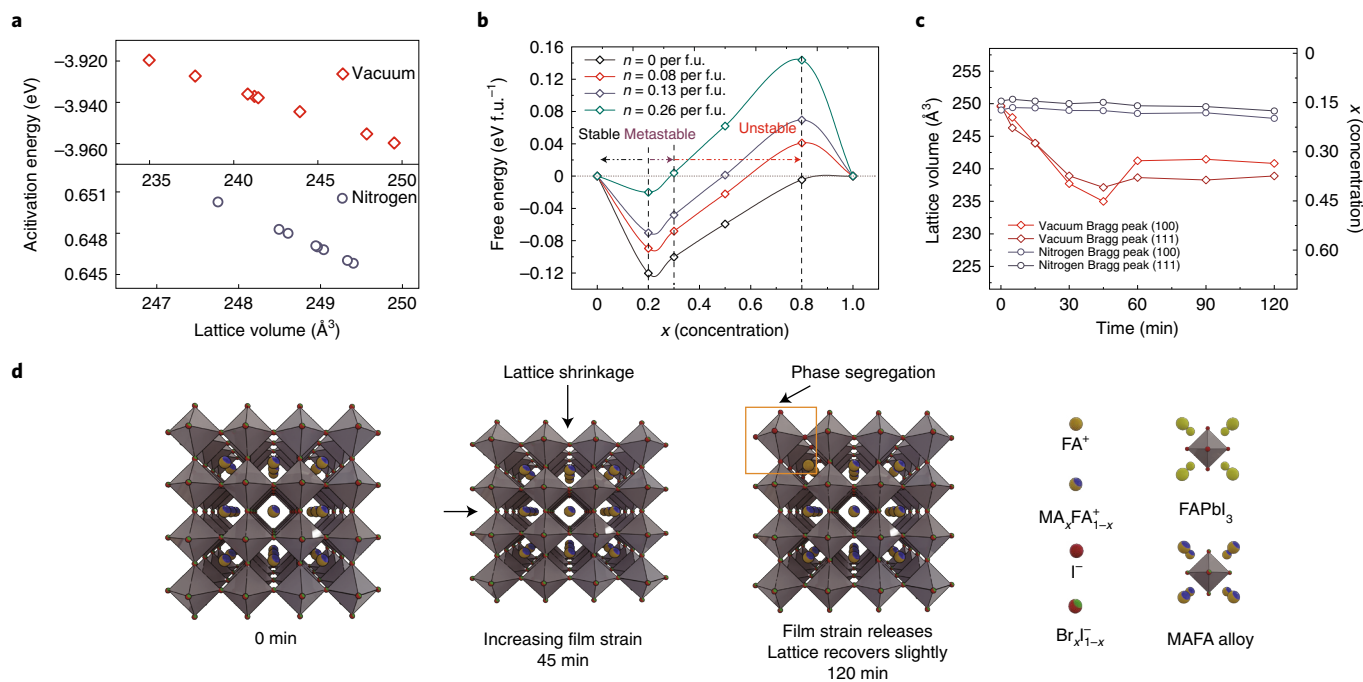


Fig. 4 | The thermodynamic driving force of lattice shrinkage and phase segregation. **a**, Evolution of activation energies for phase segregation as a function of lattice volume under vacuum (red) and a nitrogen atmosphere (blue). **b**, Density functional theory calculated Helmholtz free energy ΔF_{mix}^* of $(\text{MAPbBr}_3)_x(\text{FAPbI}_3)_{1-x}$ ($x = 0, 0.2, 0.3, 0.5, 0.8$ and 1) at room temperature ($T = 300$ K) for different photoexcited charge carrier densities, n . The black, purple and red dashed lines indicate the stable, metastable and unstable phase for different compositions of the perovskite, respectively. f.u. refers to formula unit. **c**, The lattice volume evolution translated to related compositional ratios as a function of the operation time in different atmospheres. **d**, Schematic diagram projecting the non-uniform lattice shrinkage during the operation of PSCs in vacuum, followed by the phase segregation of the MAFA perovskite, which is highlighted by an orange frame.

means of the method used in the references, to show the potential for phase segregation³³.

We find negative activation energies of the MAFA perovskite under operation in vacuum, indicating that the phase segregation could occur spontaneously at room temperature (Fig. 4a). In contrast, a positive activation energy for operation in nitrogen indicates a much larger energy barrier for the phase segregation, efficiently preventing phase segregation. Figure 4b shows that perovskites with different components display different thermodynamic phase stabilities. When the free energy of the mixing perovskite phase (ΔF_{mix}) is larger than 0, phase segregation is energetically favourable for the corresponding secondary phases. Additionally, the phase segregation energy (ΔF_{sep}) for different concentrations x for $(\text{MAPbBr}_3)_x(\text{FAPbI}_3)_{1-x}$ illustrates a concave upward curvature of ΔF_{mix} ranging from $x = 0$ to $x = 0.2$, indicating a thermodynamically stable mixed phase at room temperature. The concave downward curvature of ΔF_{mix} from $x > 0.2$ refers to metastable ($\Delta F_{\text{mix}} < 0$) and unstable states ($\Delta F_{\text{mix}} > 0$) for the MAFA perovskite. However, ΔF_{mix} will increase if we take the influence of photoexcited carriers ($n = 0 - 0.26$ per formula unit) into consideration, and this results in a thermodynamic driving force for the phase segregation of the perovskite film¹¹. This observation is also consistent with previous reports, which pointed out that perovskite materials tend to be phase separated as the Br content increases^{23,37}.

Next, we link the thermodynamic kinetics with the structure and morphology evolution process. Figure 4c shows the lattice volume as a function of the composition ratio of MAPbBr_3 and FAPbI_3 . We calculate it by using the crystallographic information file (Supplementary Tables 1–4). Corresponding changes of MAFA perovskite lattice volumes as a function of operation time in different atmospheres are also taken into consideration.

Under vacuum, the operation of PSCs demonstrates a strong lattice shrinkage to suppress the trend of spontaneous phase segregation at room temperature (Fig. 4a and Supplementary Fig. 7a). After a 45-min operation in vacuum, the lattice volume reaches about 235 \AA^3 , which is the expected value for the lattice volume of the component $(\text{MAPbBr}_3)_{0.45}(\text{FAPbI}_3)_{0.55}$. Hence, the film strain increases dramatically due to such lattice shrinkage. The dramatically compressed lattices perturb the balance between the film strain and the phase stability. The intrinsically different crystal-lite orientations for the MAFA phase and FAPbI_3 offer a starting point for phase segregation. To maintain the metastability of the $(\text{MAPbBr}_3)_{0.17}(\text{FAPbI}_3)_{0.83}$ PSCs during operation in vacuum, FAPbI_3 crystals precipitate from the (210) habit plane, thereby releasing the film strain (Fig. 2e and Supplementary Fig. 8c). This process also forms a coherent phase boundary, which could increase the strength of the perovskite film and suppress further phase segregation. Moreover, small-size crystals break, to maintain the low energy of the whole system, and thus introduce a grain-boundary strengthening. Finally, the lattice volume reaches approximately 240 \AA^3 , which is the expected value for the component $(\text{MAPbBr}_3)_{0.28}(\text{FAPbI}_3)_{0.72}$. This component has a negative value of ΔF_{mix} even under strong illumination, indicating a metastable mixed perovskite phase state.

We speculate that there are four causes for the observed phase segregation, severe lattice shrinkage and broken crystals under vacuum, as illustrated in the schemes in Figs. 3c and Fig. 4d: (1) a remarkable mismatch between the compressed lattice volume and the real components of the film; (2) intrinsically different crystal-lite orientations of the MAFA and FAPbI_3 ; (3) the need to decrease the film strain introduced by phase segregation and the formation of the coherent phase boundary; and (4) the demand to strengthen

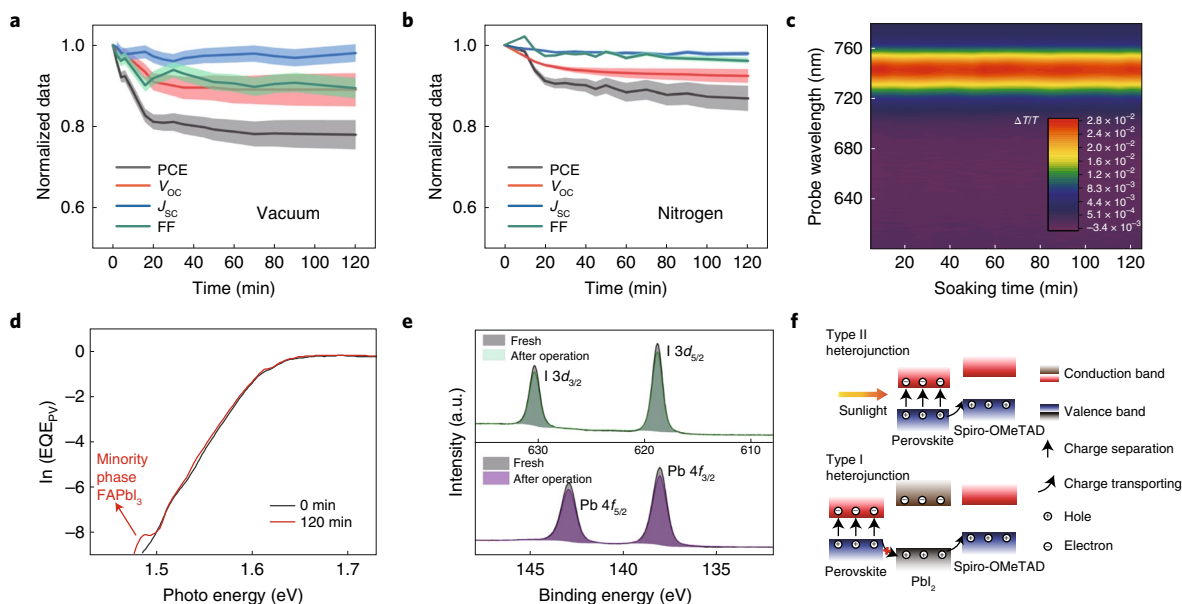


Fig. 5 | Degradation mechanisms of MAFA PSCs under the ISOS-L-1 protocol in different atmospheres. **a**, Evolution of PCE (black), J_{sc} (blue), V_{oc} (red) and FF (green) measured by the reverse scan (from 1.3 V to -0.2 V) under vacuum. **b**, Evolution of PCE, J_{sc} , V_{oc} and FF measured by the reverse scan in nitrogen. For **a** and **b**, the shaded areas indicate error bars extracted from the standard deviation of normalized PCE, J_{sc} , V_{oc} and FF values of six devices operated under the ISOS-L-1 protocol in different atmospheres. **c**, Transient absorption spectra (100–120 ps average) of the perovskite active layer as a function of illumination time under vacuum (3.4×10^{-3} Pa). The colour bar indicates the change in the transmission (absorption) of the broadband probe pulse when the sample is photoexcited by a pump pulse. **d**, Photovoltaic external quantum efficiencies (EQE_{PV}) of $(MAPbBr_3)_{0.17}(FAPbI_3)_{0.83}$ PSCs measured before and after operation in vacuum. **e**, The change of XPS $I 3d$ and $Pb 4f$ spectra for $(MAPbBr_3)_{0.17}(FAPbI_3)_{0.83}$ PSCs measured before and after the operation under voltage-bias conditions, and the baseline of data extracted through a Shirley background correction. **f**, Schematic illustration for the effects of the migration of PbI_2 to the interface between perovskite and spiro-OMeTAD.

the perovskite film to suppress further deformation through the increase of grain boundaries due to broken crystals.

Physical adsorption of gas molecules can decrease the free energy via an exothermic process³⁸. Thus, we speculate that the physical adsorption of nitrogen could play an important role in reducing the film strain and maintaining the lattice and phase stability, which is also related to a larger activation energy barrier for phase segregation, as discussed above. This observation is similar to the study of Alberti et al., which showed that a nitrogen-assisted process played an important role in lattice recovery during the annealing process, and that long-term operational stability can be improved by device encapsulation inside a pure nitrogen atmosphere³⁹.

Different degradation pathways and relative performance

We examined the temporal device performance of MAFA PSCs under operation conditions in the two different atmospheres. Devices operated in nitrogen show a better stability in terms of open-circuit voltage (V_{oc}), fill factor (FF) and PCE, compared with those operating under vacuum. Figure 5a shows a decrease of 20% for V_{oc} and 10% for FF under vacuum (normalized from six devices; Supplementary Fig. 12a,b shows the exemplary $J-V$ evolution from one of these devices). In contrast, PSCs show only a 10% decrease of the V_{oc} in a nitrogen atmosphere (Fig. 5b). To identify the mechanisms for these losses, we measured transient absorption spectra for a MAFA perovskite film within 120 min of exposure to a white-light spectrum under vacuum. Figure 5c shows that there is no peak shift for the perovskite film with white-light soaking under a high-vacuum condition, indicating that the decrease of V_{oc} is not due to the worse band alignment⁴⁰. Because the power of a white-light lamp is lower than that of the AM 1.5G spectrum, we executed 480-min illumination to obtain a comparable dose of illumination. Detailed analysis (Supplementary Fig. 13) suggests that

illumination is less likely to change the non-radiative relaxation of higher electronic states, vibrational relaxations and radiative relaxations of the perovskite, even after 480-min illumination.

To further confirm this finding, we measured the photovoltaic external quantum efficiencies (EQEs) for the fresh PSCs and the same PSCs after the degradation process under vacuum. Indeed, Fig. 5d shows that the feature of $FAPbI_3$, as the minority phase, appears after phase segregation. This could be due to an outgassing process of MA molecules from the perovskite layer when the PSCs are operated under vacuum⁴¹. Hence, phase segregation occurs only when PSCs are operated under vacuum, agreeing well with the GIWAXS study discussed above. This minority phase leads to an increasing charge carrier density due to energetic confinement within a small fraction of the total film volume. All charge carriers tend to funnel into the $FAPbI_3$ having the lowest band gap. This increased charge carrier density could increase the radiative recombination, given that the bimolecular radiative recombination process is much stronger than the monomolecular non-radiative recombination¹⁰. The same study suggested that the V_{oc} loss is pinned by the increasing amount of a low band gap iodide-rich phase. We executed the device simulation via SCAPS-1D on the basis of the ‘drift-diffusion’ model to simulate the effects on devices by increasing the radiative recombination coefficient of the perovskite materials⁴². Even if the radiative recombination coefficient of the MAFA perovskite increases from 3.16×10^{-12} to 3.16×10^{-6} in the simulation for the perovskite layer, there is a voltage penalty of only 26 mV (Supplementary Fig. 12c,f). Thus, the larger voltage loss observed in vacuum conditions cannot result only from phase segregation.

Given that phase segregation of PSCs does not influence the device performance strongly, we predict that there must be additional changes at interfaces affecting the final device performance notably. A previous study using advanced in situ transmission

electron microscopy revealed that the voltage-bias scan for PSCs could cause the formation of PbI_2 nanoparticles between the perovskite and the spiro-OMeTAD interface⁴³. We confirm this phenomenon via an X-ray photoemission spectroscopy (XPS) study (Fig. 5e). From a detailed quantitative analysis (see Supplementary Note 7), we find that the I/Pb ratio decreases from 3.11 to 2.71 after a continuous voltage-bias scan for 30 min. The decrease of the I/Pb ratio confirms that PbI_2 migrates into the interface between the perovskite film and spiro-OMeTAD.

We also investigated the effect of existing PbI_2 between the perovskite and the hole transport layer using a simulation of the ‘drift-diffusion’ model. We find a voltage loss of 90 mV after inserting a PbI_2 layer between the perovskite and the hole transport layer, showing that the excess PbI_2 at the interface reduces the V_{OC} dramatically (Supplementary Fig. 12d). In addition, a control experiment for PSCs without excess PbI_2 under operation in a different atmospheric condition was executed. The drop of V_{OC} for PSCs was obviously suppressed after 120 min of illumination in both vacuum and nitrogen conditions (Supplementary Fig. 14). Hence, we confirm that, under voltage-bias conditions, excess PbI_2 migrates to the interface between the perovskite and the spiro-OMeTAD layer irrespective of the type of atmosphere, thereby degrading the V_{OC} of the devices. The existence of PbI_2 changes the heterojunction type for PSCs from the staggering gap (type II) to the straddling gap (type I) because of the larger band gap of PbI_2 (Fig. 5f). This change forms a worse band alignment for transporting holes. Furthermore, the GISAXS data show that small crystals break up during operation under vacuum, which can create pinholes. This results in shunting pathways, dramatically decreasing the shunt resistance of the devices⁴⁴. From the ‘drift-diffusion’ simulation, we find that a decrease of the shunt resistance results in a decrease of the FF and the V_{OC} of the devices (Supplementary Fig. 12e). This finding supports our results of a stronger degradation during operation under vacuum. Overall, the PbI_2 migration is one mechanism, which causes voltage loss and occurs for PSCs in both atmospheres. The segregation of the minority phase and the formation of small crystals from larger crystals (~40 nm) cause an additional voltage loss and a severe FF loss during operation under vacuum.

Conclusion

We investigate the kinetics between structural changes and phase segregation, and explain them in detail with regard to thermodynamic theory. We also reveal the atmosphere-dependent degradation mechanisms for PSCs under different operation conditions. Operating PSCs under vacuum causes both a large degree of lattice shrinkage and a spontaneous process for phase segregation of the mixed-cation lead mixed-halide PSCs. Importantly, these effects are mitigated in nitrogen. Therefore, we suggest using a nitrogen atmosphere with an ambient pressure as a standard atmosphere for guiding scientific research and industrial development in the perovskite field. Furthermore, these findings provide a constructive way to improve the long-term operational stability of this emerging photovoltaic technology via nitrogen encapsulation or lattice fine-modification of perovskite materials.

Methods

Precursor preparation. The tin(IV) oxide 15% in H_2O colloidal dispersion (Alfa Aesar, catalogue no. 44592) was diluted with deionized water with a volume ratio of 1:4, and was shaken for 2 h at room temperature. The MAFA perovskite solution was prepared by first mixing the powders methylammonium bromide (22.4 mg, Greatcellolar, catalogue no. MS301000), lead bromide (73.4 mg, Alfa Aesar, catalogue no. A19406), formamidinium iodide (172 mg, Greatcellolar, catalogue no. MS150000) and lead iodide (485 mg, Sigma-Aldrich, catalogue no. 554359-5G). Then, 640 μl DMF (Acros, catalogue no. 348435000) and 160 μl DMSO (Acros, catalogue no. 348441000) were added into the mixed powders. The obtained mixture was dissolved and stirred at 70 °C for 30 min, followed by stirring at room temperature for 30 min. The solution was used within 2 h of preparation. The $\text{Cs}_{10}\text{FA}_{90}\text{PbI}_3$ perovskite solution was mixed by caesium iodide (31.2 mg, abcr,

catalogue no. AB207757), formamidinium iodide (192.6 mg) and PbI_2 (576.3 mg) in 800 μl DMF and 200 μl DMSO. The obtained solution was stirred at room temperature for 2 h. The spiro-OMeTAD solution was a mixture of spiro-OMeTAD (72.3 mg, Sigma-Aldrich, catalogue no. 902500), 1 ml chlorobenzene (Acros, catalogue no. 443001000), 17.5 μl lithium bis(trifluoromethanesulfonyl)imide (LiTFSI) (520 mg ml^{-1} , Sigma-Aldrich, catalogue no. 544094) in acetonitrile (Sigma-Aldrich, catalogue no. 2710004) and 28.8 μl 4-*tert*-butylpyridine (Sigma-Aldrich, catalogue no. 142379).

Device fabrication. We fabricated perovskite solar cells as described in previous publications^{45,46}. The patterned indium-doped tin oxide (ITO from Lumtec, catalogue no. LT-G001) substrates (25 × 25 mm^2) were immersed and washed in diluted Hellmanex III (2:98) solution (Sigma-Aldrich, catalogue no. Z805939-1EA), deionized water, acetone, isopropanol and ethanol in the ultrasonication bath for 10 min each. Then, the substrates were dried at 80 °C in the oven. Before spin-coating the diluted tin oxide solutions, the substrates were treated by oxygen plasma for 10 min with 168 W. The tin oxide solution was spin-coated at 3,000 r.p.m. (1,000 r.p.m. per second) for 30 s, followed by annealing at 150 °C for 30 min. After the substrates cooled down, the substrates were transferred into a nitrogen-filled glovebox. The perovskite precursor was spin-coated on ITO/ SnO_2 substrates at 6,000 r.p.m. (800 r.p.m. per seconds) for 30 s and we rapidly added 70 μl chlorobenzene into the centre of the substrates under a vertical angle at 5 s before ending, followed by 40–60 min annealing at 100 °C. For the $\text{Cs}_{10}\text{FA}_{90}\text{PbI}_3$ component, we slowly added 120 μl chlorobenzene into the centre of the substrates under a vertical angle at 15 s before ending, followed by 15 min annealing at 150 °C. When the substrates were cooled down, we dynamically spin-coated spiro-OMeTAD solution on ITO/ SnO_2 /perovskite substrates at 4,000 r.p.m. for 20 s. Then, all the substrates were stored in a dark desiccator with silica gel (<10% relative humidity) for 24 h to increase the conductivity of the spiro-OMeTAD layer. Finally, an 80-nm thick Au layer was evaporated on the spiro-OMeTAD layer with 2 nm (0.2 \AA s^{-1}) and 78 nm (1.2 \AA s^{-1}) at a pressure of 10^{-5} bar. The devices were kept in the desiccator and measured regularly until the efficiency reached stable values.

Solar cell characterization. The current density–voltage (J – V) data were recorded using a Keithley 2611B source meter under the illumination of a solar simulator (class ABA) with a light intensity of 100 mW cm^{-2} , which was calibrated with a reference solar cell (Fraunhofer ISE019-2015). The solar cells were measured with a scanning speed of 50 mV s^{-1} (voltage step of 10 mV and integration time of 100 ms). There were six (or eight) gold, top electrodes with a dimension of 2.5 × 10.0 mm^2 (or 3.5 × 10.0 mm^2) for each substrate on a substrate with a size of 25 × 25 mm^2 . The active area was controlled by a metal shadow mask (0.12 or 0.19 cm^2) to avoid overestimation of the photocurrent.

The EQEs were measured by an Oriel Quantum Efficiency Measurement Kit (Newport). The light source spectrum response was calibrated by the silicon detector. The measurements were performed using the Oriel Instruments QEPVSI-b system with a Xenon arc lamp (Newport, 300 W, catalogue no. 66902) chopped at 30 Hz and a monochromatic instrument (Newport Cornerstone 260). The EQE was measured and normalized in the wavelength range of 350–900 nm.

Material characterization. The surface morphology was probed with a field-emission SEM (Zeiss NVision 40) with an acceleration voltage of 5 kV at a working distance of 3.5 mm. Photoluminescence spectroscopy was performed with a Picoquant Fluotime 300 spectrofluorometer, using an excitation wavelength of 370 nm. Ultraviolet–visible absorption spectra were measured using a Lambda 35 spectrometer (PerkinElmer).

Operando synchrotron radiation-based grazing-incidence small/wide-angle X-ray scattering. The operando experiments were executed at beamline P03 at Deutsches Elektronen-Synchrotron (DESY, Hamburg) during two separate beamtimes to ensure reproducibility^{47,48}. The wavelength of the monochromatic X-ray beam was set to 11.65 keV and 11.70 keV to avoid the absorption edge of lead (around 13 keV) and thus minimize X-ray radiation damage. Two-dimensional GIWAXS data were collected at an incident angle of 0.4° with a Pilatus 300K (Dectris, pixel size 172 μm) and LAMBDA 4.5M (X-Spectrum, pixel size 55 μm) detectors. Two-dimensional GISAXS data were collected at the same incident angle (0.4°) with Pilatus 1M and Pilatus 300K detectors. The parameters of beam centre and the sample-to-detector distance of GISAXS detector images were calibrated via fits of the patterns of LaB_6 powders using the DPDAK package⁴⁹. The parameters of beam centre and the sample-to-detector distance of GIWAXS detector images were calibrated via fits of the patterns of CeO_2 powders using the DPDAK package. The GISAXS detector images were further treated via the DPDAK package based on Python v.2.7. The reciprocal q -space GIWAXS scattering images, the line cuts and the azimuthal integrations of the scattering data were obtained with the GIXSGUI MATLAB plug-in⁵⁰. To calibrate the intensity of different scattering images, we normalized the intensity to the ionization energy of the incident X-ray beam for each frame.

Conditions of the synchrotron radiation-based operando grazing-incidence X-ray scattering method. The operando GIWAXS studies on the MAFA PSCs were done via the ISOS-L-II protocol (with continuous voltage-bias scan and

illumination) to unify the experimental assessment. ISOS-L-II stands for the intrinsic photostability at room temperature (similar to ISOS-L-1 except that the atmosphere is inert). The pressures were kept at 5×10^{-1} Pa for the vacuum condition and 1.01×10^5 Pa for a pure nitrogen atmosphere, respectively. The temperature of the entire operando measurement chamber was stabilized at $25.0 \pm 0.7^\circ\text{C}$ with a water-cooling system, which was monitored by an infrared thermometer.

Gas adsorption measurement. Perovskite single crystals were synthesized by the method described in previous work⁵¹. In short, methylammonium bromide (22.4 mg), lead bromide (73.4 mg), formamidinium iodide (172 mg) and lead iodide (485 mg) were dissolved in 1 ml γ -butyrolactone solution at a hotplate set at 65°C in a nitrogen glovebox, until the solution became clear. This precursor solution was annealed to 100°C to grow single-crystal seeds. A new precursor solution was used after this to obtain large crystals. The single crystal was ground to obtain perovskite powder. Nitrogen adsorption measurements were performed using a Micromeritics ASAP 2420 instrument. Before the adsorption measurements, 0.68 g perovskite powder were out-gassed at 85°C for 10 h in vacuum. The measurement was carried out in a 77-K liquid- N_2 bath.

Computational methods. The Gibbs free energy of the mixed-cation and mixed-halide hybrid perovskite $(\text{MAPbBr}_3)_x(\text{FAPbI}_3)_{1-x}$ was evaluated via

$$\Delta G(x) = \Delta U(x) - T\Delta S(x) + P\Delta V \quad (3)$$

where $\Delta U(x)$ and $\Delta S(x)$ are the mixing energy and entropy of perovskite phases, respectively. T , P and ΔV are the temperature, pressure and change in volume of the system. The mixing energy, $\Delta U(x)$, is defined as:

$$\Delta U(x) = U_x - (1-x)U_{\text{FAPbI}_3} - xU_{\text{MAPbBr}_3} \quad (4)$$

where U_x , U_{FAPbI_3} and U_{MAPbBr_3} are the calculated DFT total energies per formula unit of $(\text{MAPbBr}_3)_x(\text{FAPbI}_3)_{1-x}$ and the pure FAPbI_3 and MAPbBr_3 , respectively.

The mixing entropy was

$$\Delta S(x) = -k_B [x \ln x + (1-x) \ln(1-x)] \quad (5)$$

in which k_B is the Boltzmann constant.

Without the $P\Delta V$ term, the expression of free energy is

$$\Delta F(x) = \Delta U(x) - T\Delta S(x) \quad (6)$$

where $\Delta U(x)$ and $\Delta S(x)$ follow from equations (4) and (5).

The free energy upon illumination was estimated following the method mentioned in refs.^{41,52}. We assumed that when $(\text{MAPbBr}_3)_x(\text{FAPbI}_3)_{1-x}$ was under illumination, pairs of photogenerated charge carriers were generated uniformly in the material at a density (per formula unit) n , whereupon the free energy becomes

$$\Delta U_x^* = \Delta U_x + nE_g(x) \quad (7)$$

For the unmixed state $(1-x)\text{FAPbI}_3 + x\text{MAPbBr}_3$, it was assumed that all charge carriers funnel into the FAPbI_3 , so the total energy of photoexcited FAPbI_3 becomes

$$\Delta U_{\text{FA}}^* = \Delta U_{\text{FA}} + n \frac{1}{1-x} E_g^{\text{FA}} \quad (8)$$

Using equations (7) and (8) in equation (4), with U_x and U_{FA} substituted by U_x^* and U_{FA}^* , we obtained

$$\Delta U^*(x) = \Delta U(x) + n \left(E_g(x) - E_g^{\text{FA}} \right) \quad (9)$$

The free energy of mixing of $(\text{MAPbBr}_3)_x(\text{FAPbI}_3)_{1-x}$ under photo illumination becomes

$$\Delta F^*(x) = \Delta F(x) + n \left(E_g(x) - E_g^{\text{FA}} \right) \quad (10)$$

The slope of ΔF_{mix} refers to the phase stability of materials:

$$\Delta F_{\text{sep}} = \frac{\sigma^2 \Delta F_{\text{mix}}}{\sigma x^2} \quad (11)$$

which indicates that mixed phases are maintained as stable when the curvature is convex ($0 < x < 0.2$ in our case), while mixed phases start to separate when the curvature is concave ($0.2 < x < 1$ in our case)⁵³.

The DFT calculations were performed using the Vienna Ab initio Simulation Package (VASP) code⁵⁴. A revised Perdew–Burke–Ernzerhof generalized gradient approximation (GGA) functional (PBEsol) was used for the exchange–correlation functional⁵⁵. The supercell method was employed for the simulation of the phase $(\text{MAPbBr}_3)_x(\text{FAPbI}_3)_{1-x}$ ($x=0.2, 0.3, 0.5, 0.8$). Accordingly, $1 \times 5 \times 1$, $2 \times 2 \times 1$ and $2 \times 5 \times 1$ supercells were constructed for $x=0.2$ (0.8), 0.5, 0.7 on the basis of a 12-atom cubic unit cell of MAPbBr_3 . Then, we substituted MA cations by FA cations and Br anions by I anions at different concentrations. For these, three

and four possible configurations were considered for $(\text{MAPbBr}_3)_x(\text{FAPbI}_3)_{1-x}$ with $x=0.2$ (0.8), 0.5 and 0.7, respectively. The total energy of the configurations belonging to the same concentration was averaged to obtain the total energy for the phases (U_x). A cubic-phase crystal structure was utilized for the calculations of the pure compounds MAPbBr_3 and FAPbI_3 , which corresponds to $x=0$ and 1 in $(\text{MAPbBr}_3)_x(\text{FAPbI}_3)_{1-x}$. A plane-wave basis set with a cut-off of 500 eV was used and the convergence criterion for the total energy was set to 10^{-5} eV. All lattice vectors and atomic positions were fully relaxed until the Hellmann–Feynman forces on each atom were less than $0.01 \text{ eV } \text{\AA}^{-1}$. A Monkhorst–Pack k -point mesh with a grid spacing of $\sim 2\pi \times 0.02 \text{ \AA}^{-1}$ was used for the Brillouin zone integration. Spin–orbit coupling (SOC) was not taken into account for all calculations since preceding studies noted that the band gap calculated using GGA (PBE or PBEsol) without SOC showed reasonable agreement with the experimental band gap due to a cancellation of errors^{56–58}.

The activation energy for phase segregation was calculated using equation (12):

$$k_{\text{migration}} = \frac{e^2 N \nu_0 d^2}{6\epsilon_0 \epsilon_{\text{perovskite}} k_B T} e^{\frac{\Delta S}{k_B}} e^{-\frac{\Delta H}{k_B T}} \quad (12)$$

where ΔS represents the change in the entropy of a single-ion migration step obtained from our calculation; k_B is the Boltzmann constant; ν_0 is the attempt frequency for an ion to hop, which was extracted from the work of Ni et al.⁵⁹; d is the ionic hopping distance, which depended on the lattice parameter of the unit cell; E_a is the activation energy, which is represented here by enthalpy (ΔH). ΔH was also obtained from our DFT calculation, e is the elementary charge, $\epsilon_{\text{perovskite}}$ is the dielectric constant of the perovskite, ϵ_0 is the dielectric constant in a vacuum and N is the doping density obtained from the literature³⁴. The previous study assumed that the migration rate was largely proportional to the activation energy for the phase segregation because all the parameters, except E_a (ΔH), could be regarded as constants in the situation discussed³³. However, for our study, the doping density and the dielectric constant were changing with atmospheres and pressure under illumination. Hence, we deduced that the migration rate also changed. The activation energy was described as

$$-\ln k_{\text{migration}} = -\ln \frac{e^2 \nu_0}{6\epsilon_0 k_B T} - \ln \frac{Nd^2}{\epsilon_{\text{perovskite}}} - \frac{\Delta S}{k_B} + \frac{\Delta H}{k_B T} \quad (13)$$

The various parameters to enter into equation (13) are given in Supplementary Table 13.

Transient absorption spectroscopy at low pressure. The femtosecond 400-nm pump and white-light probe were used as the illumination source for light soaking. The white-light continuum generated by a non-collinear optical parametric amplifier consisted of a visible pulse light between 520 nm and 780 nm operated at a 1-kHz repetition rate, with an average power of $\sim 400 \mu\text{W}$. The white-light pulse was equally divided into probe and reference, before being focused onto the sample to an effective beam radius of $\sim 100 \mu\text{m}$, corresponding to an energy per pulse of $\sim 630 \mu\text{J cm}^{-2}$ for each split beam and a carrier density of $\sim 10^{20} \text{ cm}^{-3}$ at the perovskite film.

The sample film was loaded into a cube cell with spectroscopic windows on the front and back in a glovebox. Before the optical measurements, the cell was connected to a vacuum pump (HiCube 80 Eco), which was pumped overnight in the dark until the pressure stabilized at 3.4×10^{-3} Pa. The vacuum pump was kept working continuously during the measurement to ensure a stable pressure. The output of a Ti:sapphire amplifier system (Spectra-Physics Solstice Ace) operating at 1 kHz and generating ~ 100 -fs pulses was split into the pump and probe beam paths. The visible broadband beam was generated in a home-built non-collinear optical parametric amplifier (NOPA), and the white light was split into two separate beams, one probe and one reference beam. The 400-nm pump beam was created by sending the 800-nm fundamental beam of the Solstice Ace through a second harmonic-generating beta barium borate crystal of 1-mm thickness (Eksma Optics). The pump was blocked by a chopper wheel rotating at 500 Hz while a computer operated a mechanical delay stage to adjust the delay between the pump and the probe. The transmitted probe and reference pulses were collected by a silicon dual-line array detector (Hamamatsu S8381-1024Q), which was driven and read out by a custom-built board (Stresing Entwicklungsbüro).

‘Drift-diffusion’ model for device performance simulation. We used SCAPS-1D (a Solar Cell Capacitance Simulator) to build the device model with the architecture shown in Fig. 1a. Detailed parameters are illustrated in Supplementary Table 5–12 and were extracted from the literature^{60,61}.

X-ray photoelectron spectroscopy. The chemical composition of films was measured using XPS (Kratos Ultra) with an Al-K α radiation source, and all the binding energies were calibrated using carbon as a reference.

Reporting Summary. Further information on research design is available in the Nature Research Reporting Summary linked to this article.

Data availability

All data generated or analysed during this study are included in the published article and its supplementary information and source data files. The data can also be found at the following public repository: <https://doi.org/10.14459/2021mp1620140>.

Received: 2 March 2021; Accepted: 1 September 2021;
Published online: 18 October 2021

References

- Rong, Y. et al. Challenges for commercializing perovskite solar cells. *Science* **361**, eaat8235 (2018).
- Jeon, N. J. et al. Solvent engineering for high-performance inorganic–organic hybrid perovskite solar cells. *Nat. Mater.* **13**, 897–903 (2014).
- Jeon, N. J. et al. Compositional engineering of perovskite materials for high-performance solar cells. *Nature* **517**, 476–480 (2015).
- Yang, W. S. et al. Iodide management in formamidinium-lead-halide-based perovskite layers for efficient solar cells. *Science* **356**, 1376–1379 (2017).
- National Renewable Energy Laboratory *Best Research-Cell Efficiencies* <https://www.nrel.gov/pv/cell-efficiency.html> (2021).
- Cardinaletti, I. et al. Organic and perovskite solar cells for space applications. *Sol. Energy Mater. Sol. Cells* **182**, 121–127 (2018).
- Tu, Y. et al. Mixed-cation perovskite solar cells in space. *Sci. China Phys. Mech. Astron.* **62**, 974221 (2019).
- Reb, L. K. et al. Perovskite and organic solar cells on a rocket flight. *Joule* **4**, 1880–1892 (2020).
- Deretzi, I. et al. Stability and degradation in hybrid perovskites: is the glass half-empty or half-full? *J. Phys. Chem. Lett.* **9**, 3000–3007 (2018).
- Mahesh, S. et al. Revealing the origin of voltage loss in mixed-halide perovskite solar cells. *Energy Environ. Sci.* **13**, 258–267 (2020).
- Li, N. et al. Microscopic degradation in formamidinium-cesium lead iodide perovskite solar cells under operational stressors. *Joule* **4**, 1743–1758 (2020).
- Tsai, H. et al. Light-induced lattice expansion leads to high-efficiency perovskite solar cells. *Science* **360**, 67–70 (2018).
- Rolston, N. et al. Comment on ‘Light-induced lattice expansion leads to high-efficiency perovskite solar cells’. *Science* **368**, eaay8691 (2020).
- Domanski, K., Alharbi, E. A., Hagfeldt, A., Grätzel, M. & Tress, W. Systematic investigation of the impact of operation conditions on the degradation behaviour of perovskite solar cells. *Nat. Energy* **3**, 61–67 (2018).
- Khenkin, M. V. et al. Consensus statement for stability assessment and reporting for perovskite photovoltaics based on ISOS procedures. *Nat. Energy* **5**, 35–49 (2020).
- Zhou, Q. et al. High-performance perovskite solar cells with enhanced environmental stability based on a (p-FC₆H₄C₂H₄NH₂)₂[PbI₄] capping layer. *Adv. Energy Mater.* **9**, 1802595 (2019).
- Bi, D. et al. Efficient luminescent solar cells based on tailored mixed-cation perovskites. *Sci. Adv.* **2**, e1501170 (2016).
- Jesper Jacobsson, T. et al. Exploration of the compositional space for mixed lead halogen perovskites for high efficiency solar cells. *Energy Environ. Sci.* **9**, 1706–1724 (2016).
- Zhang, Y. et al. Trash into treasure: δ-FAPbI₃ polymorph stabilized MAPbI₃ perovskite with power conversion efficiency beyond 21%. *Adv. Mater.* **30**, 1707143 (2018).
- Jiang, Q. et al. Planar-structure perovskite solar cells with efficiency beyond 21%. *Adv. Mater.* **29**, 1703852 (2017).
- Roose, B., Dey, K., Chiang, Y.-H., Friend, R. H. & Stranks, S. D. Critical assessment of the use of excess lead iodide in lead halide perovskite solar cells. *J. Phys. Chem. Lett.* **11**, 6505–6512 (2020).
- Beal, R. E. et al. Structural origins of light-induced phase segregation in organic–inorganic halide perovskite photovoltaic materials. *Matter* **2**, 207–219 (2020).
- Hoke, E. T. et al. Reversible photo-induced trap formation in mixed-halide hybrid perovskites for photovoltaics. *Chem. Sci.* **6**, 613–617 (2015).
- Banerjee, S. & Mukhopadhyay, P. *Pergamon Materials Series: Phase Transformations* Vol. 12, 783–800 (Pergamon, 2007).
- Gleiter, H. in *Physical Metallurgy* 4th edn (eds Cahn, R. W. & Haasen, P.) 843–942 (North-Holland, 1996).
- Lu, K., Lu, L. & Suresh, S. Strengthening materials by engineering coherent internal boundaries at the nanoscale. *Science* **324**, 349–352 (2009).
- Jariwala, S. et al. Local crystal misorientation influences non-radiative recombination in halide perovskites. *Joule* **3**, 3048–3060 (2019).
- Lin, Y.-H. et al. A piperidinium salt stabilizes efficient metal-halide perovskite solar cells. *Science* **369**, 96–102 (2020).
- Agnew, S. R. in *Advances in Wrought Magnesium Alloys* (eds Bettles, C. & Barnett, M.) 63–104 (Woodhead Publishing, 2012).
- Eperon, G. E. et al. The role of dimethylammonium in bandgap modulation for stable halide perovskites. *ACS Energy Lett.* **5**, 1856–1864 (2020).
- Brunauer, S., Deming, L. S., Deming, W. E. & Teller, E. On a theory of the van der Waals adsorption of gases. *J. Am. Chem. Soc.* **62**, 1723–1732 (1940).
- Hutter, E. M. et al. Thermodynamic stabilization of mixed-halide perovskites against phase segregation. *Cell Rep. Phys. Sci.* **1**, 100120 (2020).
- Muscarella, L. A. et al. Lattice compression increases the activation barrier for phase segregation in mixed-halide perovskites. *ACS Energy Lett.* **5**, 3152–3158 (2020).
- Hu, Z. et al. The impact of atmosphere on energetics of lead halide perovskites. *Adv. Energy Mater.* **10**, 2000908 (2020).
- Juarez-Perez, E. J. et al. Photoinduced giant dielectric constant in lead halide perovskite solar cells. *J. Phys. Chem. Lett.* **5**, 2390–2394 (2014).
- Ahmadi, M. et al. Environmental gating and galvanic effects in single crystals of organic–inorganic halide perovskites. *ACS Appl. Mater. Interfaces* **11**, 14722–14733 (2019).
- Wang, X. et al. Suppressed phase separation of mixed-halide perovskites confined in endotaxial matrices. *Nat. Commun.* **10**, 695 (2019).
- Erkey, C. in *Supercritical Fluid Science and Technology* Vol. 1 (ed. Erkey, C.) 41–77 (Elsevier, 2011).
- Alberti, A. et al. Nitrogen soaking promotes lattice recovery in polycrystalline hybrid perovskites. *Adv. Energy Mater.* **9**, 1803450 (2019).
- Correa Baena, J. P. et al. Highly efficient planar perovskite solar cells through band alignment engineering. *Energy Environ. Sci.* **8**, 2928–2934 (2015).
- Jiang, Y. et al. Mitigation of vacuum and illumination-induced degradation in perovskite solar cells by structure engineering. *Joule* **4**, 1087–1103 (2020).
- Burgelman, M., Nollet, P. & Degraeve, S. Modelling polycrystalline semiconductor solar cells. *Thin Solid Films* **361–362**, 527–532 (2000).
- Jeangros, Q. et al. In situ TEM analysis of organic–inorganic metal-halide perovskite solar cells under electrical bias. *Nano Lett.* **16**, 7013–7018 (2016).
- Kaenung, P. et al. How contact layers control shunting losses from pinholes in thin-film solar cells. *J. Phys. Chem. C* **122**, 27263–27272 (2018).
- Jiang, Q. et al. Enhanced electron extraction using SnO₂ for high-efficiency planar-structure HC(NH₂)₂PbI₃-based perovskite solar cells. *Nat. Energy* **2**, 16177 (2016).
- Saliba, M. et al. How to make over 20% efficient perovskite solar cells in regular (n–i–p) and inverted (p–i–n) architectures. *Chem. Mater.* **30**, 4193–4201 (2018).
- Buffet, A. et al. P03, the microfocus and nanofocus X-ray scattering (MiNaXS) beamline of the PETRA III storage ring: the microfocus endstation. *J. Synchrotron Radiat.* **19**, 647–653 (2012).
- Chen, W. et al. Operando structure degradation study of PbS quantum dot solar cells. *Energy Environ. Sci.* **14**, 3420–3429 (2021).
- Gunthard, B., Wolfgang, W., Chenghao, L., Stephan, V. R. & Peter, F. A customizable software for fast reduction and analysis of large X-ray scattering data sets: applications of the new DPDAK package to small-angle X-ray scattering and grazing-incidence small-angle X-ray scattering. *J. Appl. Crystallogr.* **47**, 1797–1803 (2014).
- Jiang, Z. GIXSGUI: a MATLAB toolbox for grazing-incidence X-ray scattering data visualization and reduction, and indexing of buried three-dimensional periodic nanostructured films. *J. Appl. Crystallogr.* **48**, 917–926 (2015).
- Xie, L.-Q. et al. Understanding the cubic phase stabilization and crystallization kinetics in mixed cations and halides perovskite single crystals. *J. Am. Chem. Soc.* **139**, 3320–3323 (2017).
- Draguta, S. et al. Rationalizing the light-induced phase separation of mixed halide organic–inorganic perovskites. *Nat. Commun.* **8**, 200 (2017).
- Clerc, D. G. & Cleary, D. A. Spinodal decomposition as an interesting example of the application of several thermodynamic principles. *J. Chem. Educ.* **72**, 112 (1995).
- Kresse, G. & Furthmüller, J. Efficient iterative schemes for ab initio total-energy calculations using a plane-wave basis set. *Phys. Rev. B* **54**, 11169–11186 (1996).
- Perdew, J. P. et al. Restoring the density-gradient expansion for exchange in solids and surfaces. *Phys. Rev. Lett.* **100**, 136406 (2008).
- Umari, P., Mosconi, E. & De Angelis, F. Relativistic GW calculations on CH₃NH₃PbI₃ and CH₃NH₃SnI₃ perovskites for solar cell applications. *Sci. Rep.* **4**, 4467 (2014).
- Brivio, F., Butler, K. T., Walsh, A. & van Schilfhaarde, M. Relativistic quasiparticle self-consistent electronic structure of hybrid halide perovskite photovoltaic absorbers. *Phys. Rev. B* **89**, 155204 (2014).
- Thind, A. S., Huang, X., Sun, J. & Mishra, R. First-principles prediction of a stable hexagonal phase of CH₃NH₃PbI₃. *Chem. Mater.* **29**, 6003–6011 (2017).
- Ni, Z. et al. Resolving spatial and energetic distributions of trap states in metal halide perovskite solar cells. *Science* **367**, 1352 (2020).
- Calado, P. et al. Evidence for ion migration in hybrid perovskite solar cells with minimal hysteresis. *Nat. Commun.* **7**, 13831 (2016).
- Miyata, A. et al. Direct measurement of the exciton binding energy and effective masses for charge carriers in organic–inorganic tri-halide perovskites. *Nat. Phys.* **11**, 582–587 (2015).

Acknowledgements

Financial support from Deutsche Forschungsgemeinschaft (DFG, German Research Foundation) via Germany's Excellence Strategy – EXC 2089/1 – 390776260 (e-conversion) and via International Research Training Group 2022 Alberta/Technical University of Munich International Graduate School for Environmentally Responsible Functional Materials (ATUMS), as well as from TUM.solar in the context of the Bavarian Collaborative Research Project Solar Technologies Go Hybrid (SolTech) is acknowledged. L.D. thanks the Cambridge Trust and R.G., W.C., L.D., N.L., T.X. and S. Liang acknowledge financial support from the Chinese Scholarship Council (CSC). S.P. acknowledges support from the TUM International Graduate School of Science and Engineering (IGSSE) via the GreenTech Initiative Interface Science for Photovoltaics (ISPV) of the EuroTech Universities, the excellence cluster Nanosystems Initiative Munich (NIM) and the Centre for NanoScience (CeNS). K.J. and S.D.S. acknowledge the Royal Society (UF150033) for funding. We acknowledge the Engineering and Physical Sciences Research Council (EPSRC) for funding (EP/R023980/1). This work was supported by the European Research Council (ERC) under the European Union's Horizon 2020 research and innovation programme (HYPERION, grant agreement number 756962).

Author contributions

R.G. provided conceptualization, methodology, formal analysis, investigation, resources, data curation, writing (original draft), project administration and visualization. D.H. and H.E. performed investigation and formal analysis for density function calculation and writing (original draft). W.C. provided resource and investigation for beamtime and supervision. L.D. performed investigation and formal analysis for transient absorption spectra and writing (original draft). K.W. carried out validation and provided resources for the project. K.J. and S.D.S. provided resources and investigation for transient

absorption spectra. Q.X. and P.G. contributed resources and investigations for X-ray photoelectron spectroscopy. S. Li and M.Y. provided resources and investigation for Brunauer–Emmett–Teller measurements. L.K.R. contributed software and resources. M.A.S., S.P., S.Y., N.L., T.X. and A.L.O. provided resources and investigation for the beamtime. S. Liang and C.L.W. provided visualizations. N.C.G. and R.F. carried out investigation and formal analysis for transient absorption spectra. M.S. and S.V.R. provided resources, investigation, methodology and curation for the beamtime. P.M.-B. provided conceptualization, funding acquisition, project administration and validation. All authors contributed to writing, review and editing.

Competing interests

S.D.S. is a co-founder of Swift Solar. All other authors declare no competing interests.

Additional information

Supplementary information The online version contains supplementary material available at <https://doi.org/10.1038/s41560-021-00912-8>.

Correspondence and requests for materials should be addressed to Peter Müller-Buschbaum.

Peer review information *Nature Energy* thanks Antonino La Magna, Michael McGehee and the other, anonymous, reviewer(s) for their contribution to the peer review of this work.

Reprints and permissions information is available at www.nature.com/reprints.

Publisher's note Springer Nature remains neutral with regard to jurisdictional claims in published maps and institutional affiliations.

© The Author(s), under exclusive licence to Springer Nature Limited 2021

Solar Cells Reporting Summary

Nature Research wishes to improve the reproducibility of the work that we publish. This form is intended for publication with all accepted papers reporting the characterization of photovoltaic devices and provides structure for consistency and transparency in reporting. Some list items might not apply to an individual manuscript, but all fields must be completed for clarity.

For further information on Nature Research policies, including our [data availability policy](#), see [Authors & Referees](#).

► Experimental design

Please check: are the following details reported in the manuscript?

1. Dimensions

- Area of the tested solar cells Yes No Line 355. Areas of 0.12 and 0.19 cm² were used in this work.
- Method used to determine the device area Yes No Aluminium aperture masks were used during the J-V measurement, and optical microscope was used to determine the mask area.

2. Current-voltage characterization

- Current density-voltage (J-V) plots in both forward and backward direction Yes No Provided in the Fig. 1b
- Voltage scan conditions Yes No Line 396-397. The solar cells were measured with a scanning speed of 50 mVs-1 (voltage step of 10 mV and dwell time of 100 ms).
For instance: scan direction, speed, dwell times
- Test environment Yes No Device performance was measurement in air (RH<40 %), operando studies were executed under vacuum and nitrogen.
For instance: characterization temperature, in air or in glove box
- Protocol for preconditioning of the device before its characterization Yes No No preconditioning was used in this work.
- Stability of the J-V characteristic Yes No We focus on the degradation mechanism of perovskite solar cell, and we also consider the initial stage degradation.
Verified with time evolution of the maximum power point or with the photocurrent at maximum power point; see ref. 7 for details.

3. Hysteresis or any other unusual behaviour

- Description of the unusual behaviour observed during the characterization Yes No Minor hysteresis was observed for our device (see Supplementray Fig.2 a).
- Related experimental data Yes No J-V curves under reverse and forward scans were provided (see Supplementray Fig.2 a).

4. Efficiency

- External quantum efficiency (EQE) or incident photons to current efficiency (IPCE) Yes No We focus on the degradation mechainsm of perovksite solar cells instead of boosting PCE. Absolute efficiencies are not necessary to draw our conclusions.
- A comparison between the integrated response under the standard reference spectrum and the response measure under the simulator Yes No As above.
- For tandem solar cells, the bias illumination and bias voltage used for each subcell Yes No N.A.

5. Calibration

- Light source and reference cell or sensor used for the characterization Yes No Line 393-396. . We used a class ABA Xenon lamp solar simulator (LOT Quantum Design LS0500) to simulate the global AM1.5 irradiation. We calibrated and verified the intensity directly before and after the solar cell measurements with a certified KG5 filtered silicon solar cell (Fraunhofer ISE).

Confirmation that the reference cell was calibrated and certified	<input checked="" type="checkbox"/> Yes <input type="checkbox"/> No	The reference cells were calibrated by Fraunhofer ISE and explained in Method.
Calculation of spectral mismatch between the reference cell and the devices under test	<input type="checkbox"/> Yes <input checked="" type="checkbox"/> No	The light spectrum used for measurements can match with the reference silicon cell, and we did not calculate the spectral mismatch between the reference cell and the tested devices.
6. Mask/aperture		
Size of the mask/aperture used during testing	<input checked="" type="checkbox"/> Yes <input type="checkbox"/> No	Metal mask with 0.12 and 0.19 cm ² were used in this work.
Variation of the measured short-circuit current density with the mask/aperture area	<input type="checkbox"/> Yes <input checked="" type="checkbox"/> No	We measured all devices with masks.
7. Performance certification		
Identity of the independent certification laboratory that confirmed the photovoltaic performance	<input type="checkbox"/> Yes <input checked="" type="checkbox"/> No	We focus on the degradation study.
A copy of any certificate(s) <i>Provide in Supplementary Information</i>	<input type="checkbox"/> Yes <input checked="" type="checkbox"/> No	As above.
8. Statistics		
Number of solar cells tested	<input checked="" type="checkbox"/> Yes <input type="checkbox"/> No	Line 283. For operando degradation study, we measured 6 devices under each condition (vacuum and nitrogen).
Statistical analysis of the device performance	<input checked="" type="checkbox"/> Yes <input type="checkbox"/> No	See in the Fig. 1c
9. Long-term stability analysis		
Type of analysis, bias conditions and environmental conditions <i>For instance: illumination type, temperature, atmosphere humidity, encapsulation method, preconditioning temperature</i>	<input checked="" type="checkbox"/> Yes <input type="checkbox"/> No	We degraded our solar cells with the ISOS-L-1 protocol under vacuum and a nitrogen atmosphere. More details were offered in method section.